Journal of Catalysis 404 (2021) 348–361

Contents lists available at ScienceDirect

Journal of Catalysis

journal homepage: www.elsevier.com/locate/jcat

Morphology alteration of nickel microstructures for glycerol electrooxidation

Mohamed S.E. Houache [a], Mario G. Sandoval [b], Reza Safari [c], Francisco Gaztañaga [b], Federico Escudero [b], Alfonso Hernández-Laguna [d], Claro Ignacio Sainz-Díaz [d], Gianluigi A. Botton [c], Paula V. Jasen [b], Estela A. González [b], Alfredo Juan [b,*], Elena A. Baranova [a,*]

[a] Department of Chemical and Biological Engineering, Centre for Catalysis Research and Innovation (CCRI), University of Ottawa, 161 Louis-Pasteur, Ottawa, ON K1N 6N5, Canada
[b] Instituto de Física del Sur (IFISUR), Departamento de Física, Universidad Nacional del Sur (UNS), CONICET, Av. L. N. Alem 1253, B8000CPB Bahía Blanca, Argentina
[c] Department of Materials Science and Engineering, McMaster University, 1280 Main St. W, Hamilton, ON L9H 4L7, Canada
[d] Instituto Andaluz de Ciencias de la Tierra, CSIC-UGR, Av. de las Palmeras 4, 18100 Armilla, Granada, España

ARTICLE INFO

Article history:
Received 22 July 2021
Revised 22 September 2021
Accepted 8 October 2021
Available online 18 October 2021

Keywords:
NiO_x catalysts
Glycerol electro-oxidation
PM-IRRAS
Selectivity
Nickel

ABSTRACT

Shape-controlled microstructures (triangles and urchin-like) of Ni were synthesized using polyol synthesis in the presence/absence of capping agent (polyvinilpyrrolidone, PVP). Direct visualization of crystal structure and morphology before/after electrochemical tests in KOH were characterized using electron microscopy techniques. Electrochemical characterizations illustrated that urchin-Ni-PVP has highest catalytic activity among all investigated electrocatalysts for glycerol electrooxidation reaction (GEOR). Improved activity was attributed to the surface area and the highly porous structure as identified by electron tomography analysis. All Ni shapes showed similar selectivity. DFT calculations on low-index β-NiOOH and β-$Ni(OH)_2$ planes were performed as possible surfaces present during electrochemical processes. The (001) surface is the most thermodynamically stable in both systems and has different possible terminations. For O, Ni and mixed Ni-O atoms terminations the β-NiOOH(001) present metallic behavior. DFT results show that either Ni or Ni-O exposed β-NiOOH(001) surfaces are possible scenarios for glycerol adsorption on different catalytic charged surface sites.

1. Introduction

Glycerol has various industrial applications in pharmaceutics solvents, cosmetics, food, plasticizers, beverage and food industries and direct glycerol fuel cells (DGFCs). Biodiesel is generated through *trans*-esterification reaction of triglycerides present in vegetable oil and fats, with 10 wt% of low-grade glycerol as the by-product [1–4]. Several unwanted issues are associated with the presence of glycerol in biodiesel at high concentrations, such as nozzles-clogging, poor engine performance and formation of carbon deposits [5]. Furthermore, biodiesel combustion with glycerol leads to acrolein formation, unsaturated aldehyde, which is a toxic substance that is associated with serious health problems related to digestive and respiratory systems [6]. Thus, the glycerol concentration is viewed as undesired critical parameter to determine the quality of biodiesel. In this context, fuel cells could afford a profitable answer to these issues. The application of glycerol electro-oxidation in DGFCs has gained renewed interests in the past 20 years [7] due to its high charge density ($14F·mole^{-1}$), low toxicity, high boiling point (290 °C) and high theoretical energy density ($5\ Wh·kg^{-1}$ vs. 8 and $6.1\ Wh·kg^{-1}$ for ethanol and methanol, respectively) [8,9].

Ni-based catalysts are attractive candidates for glycerol electro-oxidation due to high catalytic activity and stability in alkaline media, as well as low-price compared to the platinum group metals. In addition, Ni-based materials have been applied over the last three decades in various electrochemical processes such as photocatalysis [10,11], alkaline batteries [12], supercapacitors [13], sensors [14], electrocatalysts for various organic oxidation and fuel cells [15–17]. In all of these applications, the complexity of the nickel surface chemistry strongly impacts its catalytic activity, efficiency and performance.

Nickel behaviour is quite complex since it has several phases (Ni hydroxides and oxyhydroxides between others). Besides, Ni surfaces adsorb different species (H, O, OH and H_2O) coming from dissociation products of H_2O in stable sites [18]. The Ni hydroxides and oxyhydroxides are involved in the redox process. These com-

---

* Corresponding authors.
E-mail addresses: cajuan@uns.edu.ar (A. Juan), elena.baranova@uottawa.ca (E.A. Baranova).

https://doi.org/10.1016/j.jcat.2021.10.010
0021-9517/

pounds can be increased depending on a previous treatment, resulting in the expansion of the electrochemical active surface and the oxidation of Ni hydroxide to oxyhydroxide. The last one is an active phase for GEOR giving Ni-hydroxide and different products.[9] The redox process of the different phases of the Ni hydroxides and oxyhydroxides is schematized by *Bode et al.* diagram (scheme 1 in Supplementary Material (SM)) in 1969 [19,20]. All of the structures comprise stack layers of edge-sharing NiO_6 octahedra, differing only in their gap distance between the layers, the quantity of intercalated species (i.e. OH^-, SO_4^{-2} H_2O and CO_3^{-2}) and the stacking sequence [21–24].

Among them, α-$Ni(OH)_2$ and γ-NiOOH are relatively difficult to obtain as the intercalated species affect both phases by making them poorly crystallized with a turbostratic structure [25]. Furthermore, since α-$Ni(OH)_2$ and γ-NiOOH are related to β-Ni^{II} and β-Ni^{III} (scheme 1 in SM), and the redox pair β-$Ni(OH)_2$ and β-NiOOH proceed with small structural changes, it is essential to initially comprehend the features that characterize the fundamentals of β-phases and their different surfaces. Thus, our work will be focused on the properties of β-hydroxides and oxyhydroxides.

β-$Ni(OH)_2$ is a highly crystalline compound with ABAB oxygen stacking sequence and H atoms in a tetrahedral environment (T1 structure) and space group of $P\bar{3}m1$ (Brucite) [26,27]. The experimental lattice parameters (a = b = 3.13 Å and c = 4.66 Å) were obtained at room temperature through Rietveld refinement of neutron diffraction. Thermogravimetric studies illustrate that the weight of α- and β- hydroxides drops by 30% and 1%, respectively, at 100 ℃ , indicating the vast amount of intercalated species extant in the α-$Ni(OH)_2$ structure [28,29]. Further detailed information on β-$Ni(OH)_2$ can be obtained from infrared spectroscopy and extended X-ray absorption fine structure (EXAFS) techniques. The infrared method illustrated a sharp intense antisymmetric OH stretch at 3650 cm^{-1}, which reflects free hydroxyl group and a lack of hydrogen bond [30–32]. Another experiment on EXAFS analysis exhibited coordination shells with 6 O^{2-} ions at 2.07 Å and 6.2 Ni ions at 3.13 Å [33]. These data had similar results at different temperature of 77 K and 298 K. The EXAFS results could be elucidated in terms of the ionic radii of Ni^{2+} and O^{2-}. The ionic radius of O^{2-} with six neighbours is 1.35–1.4 Å, whereas the ionic radius of Ni^{2+} is 0.69 ± 0.01 Å [34]. Taking the average of ionic radius of O^{2-} to be 1.38 Å and sum it with Ni^{2+} will give the Ni-O bond distance of 2.07 ± 0.01 Å. In addition, X-ray diffraction shows that β-Ni$(OH)_2$ (001) is the most intense and its strength and crystallinity enhances with pH increasing [35,36]. Hence the electronic properties of β-hydroxide have also been stated to be *p*-type semiconductor with a 4 eV band gap [37,38].

The β-NiOOH structure is considered more complex than β-Ni$(OH)_2$. Based on the investigation of *Oliva et al.*, the oxygen staking sequence in β-hydroxide (ABAB) alters upon oxidation to β-oxyhydroxides (ABCA), which is similar to γ-NiOOH in terms of oxygen stacking sequence [27,39]. It has been reported that there are two main possibile β-NiOOH structure deviations from the brucite lattice structure which are related to either (i) overoxidation (forming γ-NiOOH) or (ii) uncompleted oxidation (forming β-Ni$(OH)_2$ residuals) [40], whereas other studies show no major structural alterations during redox oxidation between β-Ni^{II} and Ni^{III} [31,39,41]. EXAFS analysis exhibited two possibilities of Ni-Ni distances in β-NiOOH, which are either 3.13 Å (assortment of Ni^{2+} and Ni^{4+}) [42] or 2.82 Å (Ni^{3+} in distorted octahedra) [43]. In relation to the electronic properties, β-NiOOH has been reported to be either *n*-type or *p*-type semiconductor [44,45]. DFT solid-state calculations found out an OH staggered structure with the O octahedra in between and with null dipolar moment [25]. Thus, no final conclusion was drawn regarding the properties of β-oxyhydroxides since many questions are still unanswered

In this work, a combination of electron microscopy and electrochemistry is employed to observe the surface transformation of nickel to Ni hydroxide during cyclic voltammetry in KOH. Then, we report the GEOR on triangular Ni and urchin-like Ni nanoscale particles in the presence and absence of a capping agent as polyvinilpyrrolidone (PVP). *I*n-situ (PM-IRRAS) analysis was carried out to identify the reaction products at various applied potentials. As mentioned before, during the electrooxidation process in the Ni-based electrode, the first step is the electrochemical oxidation of the hydroxide to the oxyhydroxide phase, and then, after the reaction occurs, the hydroxide is the resting state. The rate of this process makes it very difficult to characterize the oxyhydroxide surfaces. To provide a further insight on the possible surfaces involved in the process, theoretical DFT calculations were performed. We first modeled the β-$Ni(OH)_2$ and β-NiOOH bulk phases (henceforth collectively termed NiOx). Then, we analyzed the low-index surfaces of these NiOx compounds at an energetic level, considering the geometrical and electronic structure. Furthermore, the different atom expose surfaces were also searched. The determination of the most likely exposed surfaces of β-NiOOH is crucial to identify the surface's key features that enable glycerol adsorption and reaction. Our calculations show that the (001) cleavage surface plane is the most thermodynamically stable in both systems. This surface has different possible terminations, being the most stables those that expose Ni and/or O species.

2. Experimental and computational methodology

2.1. Synthesis of different shape of Ni nanoparticles

The synthesis of Ni nanoparticles was based on previous publications [46,47] but is summarized for convenience here. Nickel (II) chloride hexahydrate (99.999%, Sigma-Aldrich) was dissolved in 50 mM ethylene glycol (99.96%, Fisher Scientific) in a three-neck flask. The solution was kept under strong magnetic stirring at 100 °C on a hot plate. After 2 min, 1.7 mL of 0.1 M solution of hydrazine hydrate (50–60% purity; degree of hydration, ~1.5, Sigma-Aldrich) was added, and the color altered to sky-blue, indicating the formation of Ni-hydrazine complex. When 1.5 mL of 0.1 M NaOH (97%, Fisher Scientific) was injected to the mixture, the color of the reaction slowly turned to black indicating the formation of nickel nanoparticles (Ni NPs) based on the following reaction 1:

$$2Ni^{2+} + N_2H_4 + 4OH^- \rightarrow 2Ni + N_2 + 4H_2O \quad (1)$$

The solution was kept under stirring at 100 °C for 30 min to ensure reaction completion, and then cooled down to room temperature. A permanent magnet was used to recover Ni NPs from the solution; NPs were then rinsed with ethanol three times and separated by centrifugation at 6000 rpm for 10 min and stored in ethanol. Similar procedure was followed for Urchin-like NPs in the absence and the presence of 0.5g capping agent PVP-, where the concentration of NaOH was increased to 0.5 M NaOH.

2.2. Physicochemical characterization

Powder X-ray diffraction (XRD) patterns were collected with a Rigaku Ultima IV multi-purpose diffractometer with Cu Kα radiation (λ = 1.5418A) at 40 kV and 44 mA in the 2θ range of 20–80°. High-Resolution Scanning Electron Microscopy (HRSEM) was performed with a FEI Magellan-400 microscope operating from 1 to 30 kV. Transmission Electron Microscopy (TEM) was carried out with a Philips CM12 TEM operating at 120 kV for selected area electron diffraction (SAED) analysis with a selected area aperture (10 μm) to provide lattice spacing information on the particles.

For High-Resolution TEM (HRTEM), electron tomography and energy-filtered imaging, a FEI Titan 80–300 microscope operated at 200 kV was used. In addition, all HRTEM data were analyzed, using Gatan's Microscopy Suite Digital Micrograph software for colour coding display based on Fourier filtering of images to identify the different phases. Furthermore, tomography results were processed using Image J and Inspect 3D software for image processing and TomViz software for 3D Visualization. For the HRSEM visualization, in combination with electrochemical experiments (i.e. comparing the same samples before and after cycling), the Ni nanoparticles samples were drop-cast on stainless steel sheets which were then used as working electrodes and observed in the pristine state, then as electrochemically cycled. Platinum electrodes and Ag/AgCl were used as counter and reference electrodes, respectively. Cyclic voltammetry was carried out in 1 M KOH between 0.1 and 0.6 V vs. Ag/AgCl with a scan rate of 20 mV s^{-1} using a Gamry Reference 600 + Potentiostat.

2.3. Electrochemical and in-situ polarization modulation infrared spectroscopy (PM-IRRAS) characterization

The details of electrochemical and spectro-electrochemical characterization techniques have been reported in our previous work [9,47,48]. In summary, the following methods were used:

- All electrochemical measurements were performed in a Teflon three-electrode electrochemical cell using the potentiostat (Bio-Logic Science Instruments SAS, Claix, France) at room temperature. All potentials were measured with respect to (Hg/HgO), but reported versus the reversible hydrogen electrode (E_{RHE} =-$E_{Hg/HgO}$ + 0.855 vs RHE), unless otherwise stated.
- In-situ PM-IRRAS measurements were equipped with PMA-50 XL chamber and in-house designed spectro-electrochemical cell [9]. Before initiating the experiment, the system was purged with dry air and N_2 for 1.5 h to remove all atmospheric H_2O and CO_2 interferences.

2.4. Computational methods

As mentioned in the Introduction, experimental results indicate that at the beginning of the electrochemical reaction β-$Ni(OH)_2$ phase is present and that during the reaction course β-NiOOH could be formed. For these reasons we used these structures as the starting point for the simulation.

All calculations were performed using spin-polarized DFT-based within the all-electron, frozen-core projector-augmented-wave (PAW) formalism [49,50] with periodic boundary conditions as implemented in VASP code [51,52]. The Perdew – Burke – Ernzerhof (PBE) functional in generalized gradient approximation (GGA) for the exchange–correlation functional [53] was used. Plane-wave basis set, with a cutoff energy of 750 eV was considered. All the structures have been optimized until the forces acting in each atom are less than 10^{-4} eV/Å and the energy convergence is less than 1 meV. It well known that standard DFT fails on the description of transition metals oxides as a result of spurious self-repulsion and the missing derivative discontinuity in the exchange–correlation functional that lead to over delocalization of electrons. Then, the Hubbard correction as implemented by *Dudarev et al.* was used to partially correct these problems [54]. An effective U of 5.5 eV was used for the Ni(III) 3d orbitals, derived from linear response theory, which was taken from ref [43,55]. A Γ-point-centered Monkhorst-Pack k-point meshes of 6 × 6 × 4 and 5 × 5 × 3 for β-$Ni(OH)_2$ and β-NiOOH, respectively [56] was considered.

For the bulk model of the β-$Ni(OH)_2$ phase we use its usual brucite-type structure made of hexagonal OH-Ni-OH tri-layer sheets superimposed in simple stacking of 1H-type (T1), with a ABAB oxygen stacking sequence and hydrogen in a tetrahedral environment [57,58]. In the case of β-NiOOH phase, usually obtained in an ill-crystallized state, its structure is not well characterized in the literature. Considering that numerous previous studies suggest that the oxidation of nickel hydroxide proceeds without major structural modifications [59–61], we chose a representative $P\bar{3}m1$ (brucite) structure to model β-NiOOH. Besides this, one must choose where to locate the H atoms forming the OH groups. In this work we considered the most likely β-NiOOH structure formed upon the complete oxidation of β-$Ni(OH)_2$ with the staggered hydrogen arrangement. In all layers of this configurations, the H are equally distributed at each side, being arranged in such way that all Ni atoms have a $NiO_3(OH)_3$ coordination sphere as suggested by *Tkalych et al* [25].

Is well known that the larger clusters, with many thousands of atoms and diameters, in the range of 10 nm and more, have a smoothly varying behavior, which tends to the bulk limit as size increases [62–64], then is possible to model this NP with a surface slab. Therefore, and considering that the exposed plane is difficult to be. Experimentally determined during the reaction, we modeled several low-index planes to predict the most stable surfaces of β-Ni$(OH)_2$ and β-NiOOH phases: (100), (010), (001), (101), (011), (111) and (102). A vacuum layer of 15 Å was introduced between the slabs, which was enough to prevent interactions between periodic images. These surfaces were modeled using a 6-layers supercell. The thickness of the slab should be such that it approaches the electronic structure of 3D bulk in their inner most layers. Only the first three layers are allowed to relax, while the three remaining layers (bulk like) were kept fixed. The relaxation of the 4th layer changes the energy less than 4 meV. The surface energy (E_{surf}) for each considered cleavage plane for both systems is computed as:

$$E_{surf1}(\xi) = \frac{1}{2S(\xi)}\left\{E^{rel}_{slab}(\xi) - N_{\xi}E_{Bulk/Atom}(\Phi)\right\} \tag{2}$$

where $S(\xi)$ is the surface area of the slab, $E^{rel}_{slab}(\xi)$ is the energy of the relaxed slab, N_{ξ} is the number of atoms in the slab ξ , $E_{Bulk/Atom}(\Phi)$ is the bulk energy per atom of the Φ system, with Φ = β-$Ni(OH)_2$ or β-NiOOH.

Regarding the electronic structure and reactivity, the d-band center (ε_d) was calculate used the Hammer-Nørskov method [65–68]:

$$\varepsilon_d = \frac{\int_{-\infty}^{\infty} E\rho(E - E_F)dE}{\int_{-\infty}^{\infty} \rho(E - E_F)dE} \tag{3}$$

with $\rho(E - E_F)$ is the DOS projected on the d-states of the metal and E_F is the Fermi energy. Bader analysis as implemented by *Tang et al.* was used to calculate electronic charges on atoms [69,70].

3. Results and discussion

3.1. Physiochemical characterization of nickel microstructures

Different shapes of Ni particles were synthesized by a facile three-step modified polyol method as shown in Fig. 1a. Initially, the Ni^{2+} precursor $NiCl_2{\cdot}6H_2O$ was reduced by hydrate hydrazine in the presence and the absence of PVP at pH 12, generating small Ni nanocrystals. Then, these particles were joined with other under the influence of the magnetic dipole interactions resulting in the formation of large Ni particles with selective spear-like branches, leading to lower magnetic anisotropic energy and surface energy.

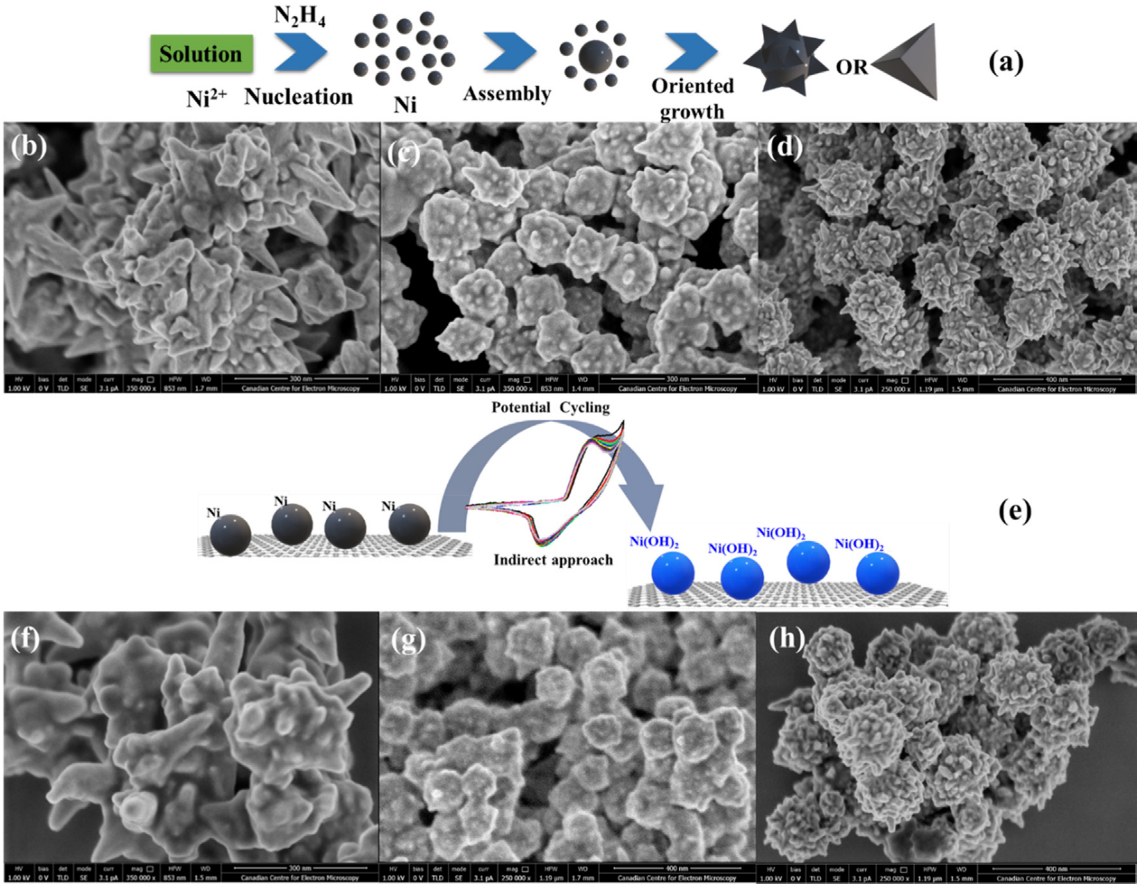

Fig. 1. (a) Illustration of the fabrication process of different Ni morphologies. SEM micrographs before (top) and after (bottom) conversion of (b,f) triangular-Ni, (c,g) urchin-Ni and (d,h) urchin-Ni with PVP to β-$Ni(OH)_2$. (e) Schematic for one-step processing of Ni hydroxide in indirect approach.

Finally, triangular and urchin-like electrocatalysts were fabricated under the influence of NaOH concentration (Fig. 1a).

The metallographic characteristics of the as-synthesized Ni particles were characterized by HRSEM (Fig. 1b-d). It is clearly seen that Ni particles have size of 100–130 nm. The crystallite particle size estimated by Debye – Scherrer's formula using the FWHM (Full Width at Half Maximum) parameter of the Ni (1 1 1) peak and the shape factor 0.9 from XRD is 20.1, 13.7 and 18.9 nm for triangular-Ni, urchin-Ni with and without PVP, respectively (Figure S1 in SM). This indicates that Ni particles were aggregated of several nanometer-sized crystallites.

The surface transformation of these three morphologies to Ni hydroxides were further investigated using in-situ HRSEM in combination with cyclic voltammetry (CV) experiments. Fig. 1e-h shows micrographs of Ni after 20 cycles in 1 M KOH between 0.1 and 0.6 V vs. Ag/AgCl at 20 mVs^{-1}. Before the conversion (Fig. 1b), Ni microstructure resembles a very sharp triangular-shaped needle-like structure. After CVs, the surface becomes much smoother with a layer covering the particles, which causes an apparent expansion (Fig. 1f). While for urchin-Ni without surfactant, the particles appear as spheres with small extrusions (Fig. 1c), resembling a sea urchin shape with short spikes as illustrated in Fig. 1g. After CVs, no traces of extrusions were visible and the surface was rather rough. Furthermore, Fig. 1d revealed that the presence of PVP in urchin-Ni allows having sharper spikes with no significant effect on nanoparticle size. However, after conversion, these spikes were no longer sharp (Fig. 1h).

Randomly chosen microparticles for TEM selected area electron diffraction (SAED) point analysis shows that each material has high polycrystallinity and a well-defined ring structure pattern (Fig. 2). Specifically, the patterns of as-synthesized materials (Fig. 2a, e and i) show evidence of a typical face-centered cubic (*fcc*) structure of Ni (1 1 1), (2 0 0) and (2 2 0) (overlayed red rings), which is in correlation with our XRD data (Figure S1 in SM). After conversion, an additional ring of Ni hydroxide crystalline planes appears (overlayed green ring) in Fig. 2-c, -g, and -k. While only, one plane seems to be strongly visible β-$Ni(OH)_2$ (1 0 2), other planes may also exist for nickel hydroxide; however, they are not detectable due to the low nickel hydroxide content, as well as their close proximity to Ni diffraction rings.

To visualize the co-existence of the two crystalline structures in real space, the microstructures of electrocatalyst were further investigated by creating a composite colour image using overlayed phases identified by the differences in crystalline structures extracted from HRTEM images, as shown are in Fig. 3. For mapping of the spatial distribution of all phases, the we used one colour channel (green) corresponding to locations of the β-$Ni(OH)_2$ as identified from Fourier filtering of the periodicity of unique lattice spacings of the β-$Ni(OH)_2$ and another colour channel (red) corresponding to the locations where only the Ni lattice spacing is detected. As seen in Fig. 3a, before conversion, the whole structure of triangular Ni was identified with Ni planes (red) with no traces of $Ni(OH)_2$, which is in a good agreement with our XRD and SAED data. However, after CV, significant amounts of nickel hydroxide (green regions) were present (Fig. 3b), which confirms the conversion. Similar trend is shown in the RGB images (Figures S2 and S3 in SM) for Urchin-like Ni in the absence and the presence of PVP.

It is worth noting that Ni planes are detected towards the core of the particles, while Ni hydroxide usually visible on the edges and tip of the particles, which is due to its contact with the electrolyte, making the surfaces easily converted. Fig. 3c illustrates the HRTEM analyses of the exact location of triangular Ni after conversion

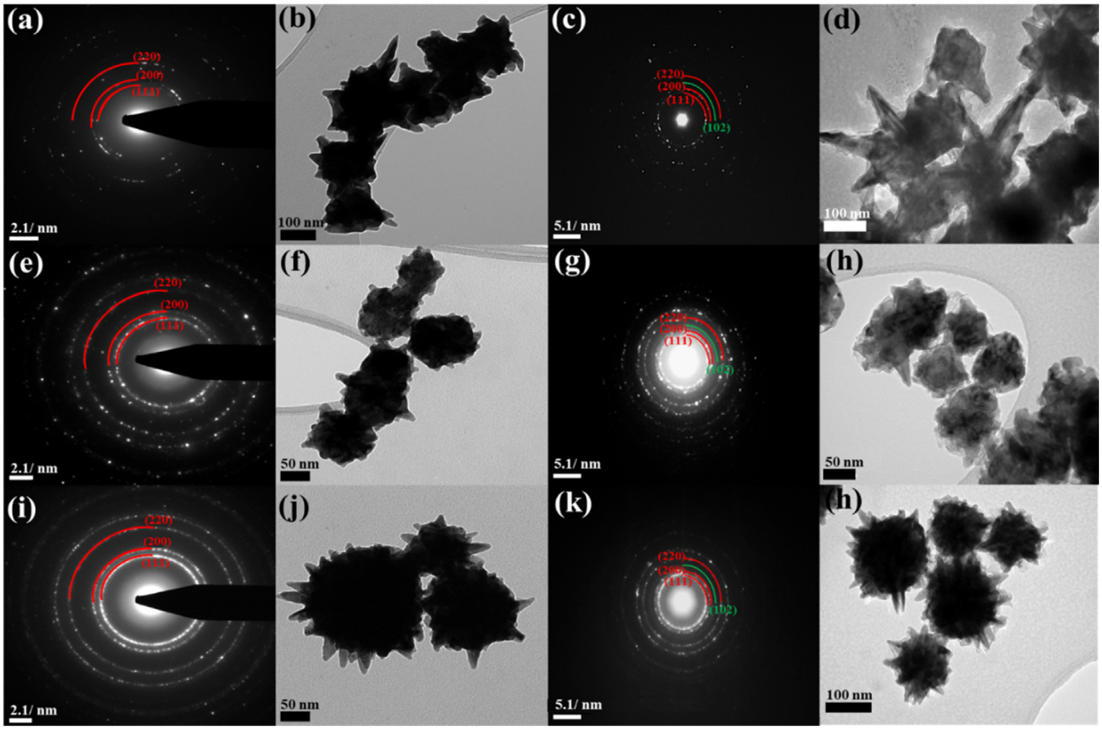

Fig. 2. SAED patterns before (left-side) and after (right-side) conversion of (a,c) triangular-Ni, (e,g) urchin-Ni and (i,k) urchin-Ni with PVP to β-Ni(OH)$_2$. Low magnification TEM images of (b,d) triangular-Ni, (f,h) urchin-Ni and (j,h) urchin-Ni with PVP.

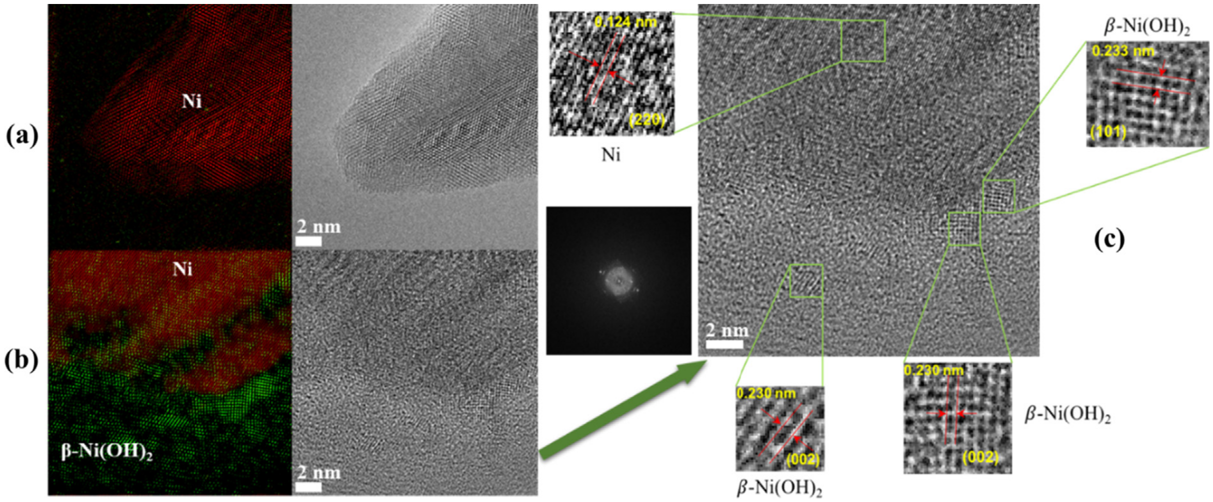

Fig. 3. (a) HRTEM and colour-coded phase micrographs (Ni in red, β-Ni(OH)$_2$ in green based on Fourier filtering of images based on the crystalline reflections unique to the two phases) of triangular-Ni (a) before and (b) after conversion. (c) Indexed HRTEM of triangular-Ni after conversion and FFT. (For interpretation of the references to color in this figure legend, the reader is referred to the web version of this article.)

(Fig. 3b), and Fast Fourier transform (FFT) analysis is used to separate the noise signal (usually high frequency) from the useful component. In order to decrease the error from the indexing of the interplanar spacing in high-resolution real space images, the crystalline planes of fcc Ni (220) and hexagonal β-Ni(OH)$_2$ (002) and (110) have been identified.

3.2. Electrochemical and in-situ PM-IRRAS measurements

Cyclic voltammograms of triangular and urchin-like Ni particles are illustrated in the cathodic region (Fig. 4a) and anodic region (Fig. 4b) in N$_2$-purged 1 M KOH. The formation of various Ni phases was well established in our previous work [9,47,48]. The reversible oxidation of Ni to α -Ni(OH)$_2$, which takes place between −0.8 and −0.4 V vs. Hg/HgO, was used to determine the electrochemical surface area (ECSA) [9,71]. The estimated ECSA of Ni catalysts is 1.36 ± 3.2%, 1.61 ± 7.2% and 1.86 ± 4.7 % cm^2 for triangular-Ni, urchin-Ni and urchin-Ni with PVP, respectively. This observation is in good correlation with the tomography analysis (Figure S4 in SM) that examines and visualizes the internal structure of nanoparticles slice by slice. After tomographic reconstruction, the presence of internal porosity is clearly identified (Figure S4 in SM). Qualitatively, from the inspection of tomograms, the porosity level for the different shapes of Ni clusters follows the order:

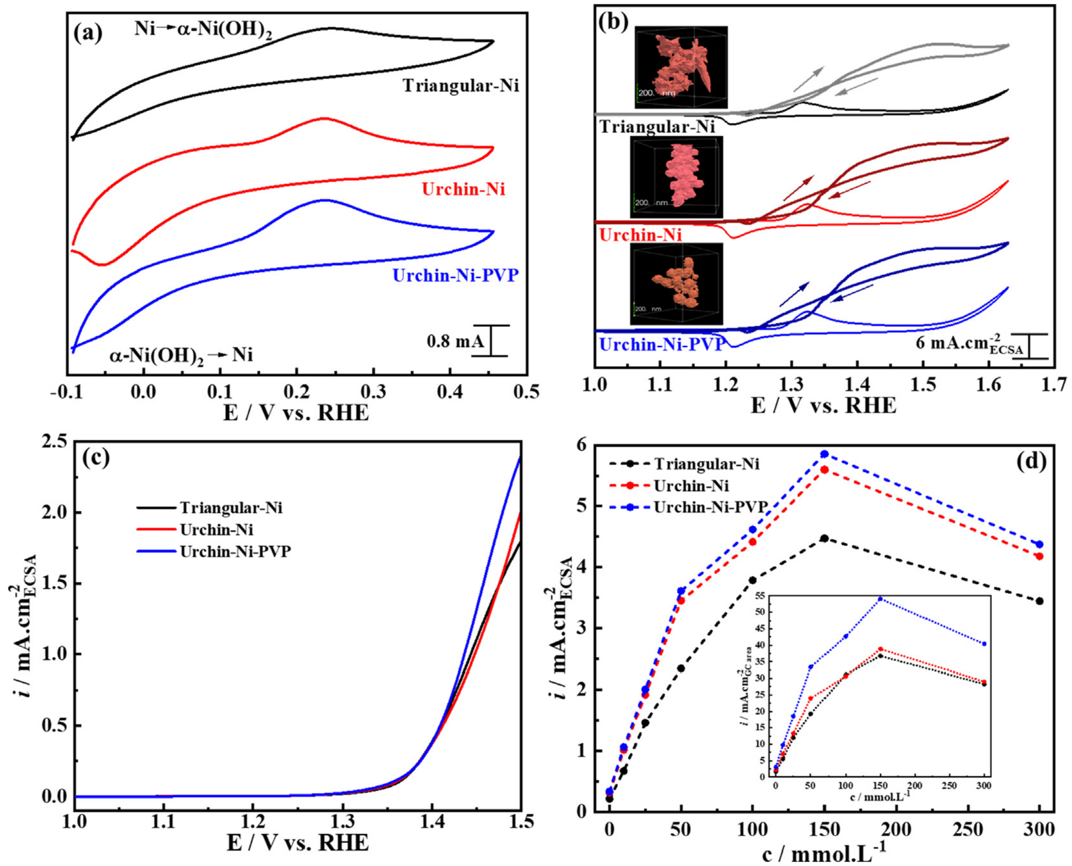

Fig. 4. Cyclic voltammograms (CVs) of Ni electrocatalysts of different shape, as indicated in the figure, in 1 M KOH (black line) and 1 M KOH + 0.1 M glycerol (red line) in the cathodic (a) and anodic (b) regions. (c) LSVs of GEOR at 1 mV.*sec*$^{-1}$ Comparison of the glycerol electro-oxidation on various glycerol concentration (d) in 1 M KOH + x mM glycerol. Scan rate 50 mV.*sec*$^{-1}$ (10th Cycle). (For interpretation of the references to color in this figure legend, the reader is referred to the web version of this article.)

urchin-like Ni with PVP has a higher porosity followed by urchin-like Ni and then triangular-Ni. Based on the above analysis, the use of polymer ligands in the synthesis seems to increase the active surface area, which is due to its structure that consists of hydrophobic portion (i.e. alkane chain). This chain is adsorbed on the surface of Ni crystal nuclei, leading to higher active sites and uniform lower surface energy that leads to evenly formed catalyst [72].

Fig. 4b shows the anodic region of CVs of Ni particles in 1 M KOH (thin line) and 0.1 M glycerol + 1 M KOH (bold line) at 50 mV *sec*$^{-1}$. The CVs in the absence of glycerol show a typical profile of Ni-based electrodes in alkaline solution [73–76]: (i) the redox pair of Ni^{2+}/Ni^{3+} in the region between ~0.3 and 0.6 V; and (ii) the oxygen evolution reaction (OER) in the region above 0.6 V vs. Hg/Hg.O. In the presence of 0.1 M of glycerol, the voltammetric profiles changes, leading to higher current density values at 0.62 V, which are 3.8 mA.cm$^{-2}_{ECSA}$ (or 31.1 mA.cm$^{-2}_{GCarea}$), 4.4 mA.cm$^{-2}_{ECSA}$ (or 30.6 mA.cm$^{-2}_{GCarea}$) and 4.7 mA mA.cm$^{-2}_{ECSA}$ (or 42.6 mA.cm$^{-2}_{GCarea}$) for triangular-Ni, urchin-Ni and urchin-Ni with PVP, respectively. In all of these catalysts, the onset potential initiates at 0.41 V vs. Hg/HgO, indicating a similar GEOR kinetics. This potential also corresponds to the beginning of β-NiOOH formation, which is an electrochemical active species for glycerol oxidation and other organic molecules known as the "indirect electron transfer mechanism" [77]. Fig. 4c shows the linear sweep voltammetry (LSV) measurements at 1 mV.*sec*$^{-1}$ indicating a similar trend in case of GEOR catalytic activity and the overpotential compared to Fig. 4b.

Fig. 4d shows the effect of different glycerol concentrations ranging from 10 to 300 mM as a function of current density at 0.62 V. At this applied potential, the catalytic activity increases with concentration up to 150 mM of glycerol, followed by a sudden drop at 300 mM. Similar behaviour was detected for all three catalysts and the catalytic activity decreased in the following order: urchin-Ni with PVP > urchin-Ni > triangular-Ni. At the same time, OER shifts towards more positive potentials when increasing the glycerol concentration as shown in Figure S5 in SM. This was mainly attributed to the strong interaction of alcohol with high valence nickel species than with OH^- species [47]. Simultaneously, the cathodic peak reduces gradually until it disappears completely at 100 mM (Figure S5 in SM). This is an indication that there is a change in the GEOR mechanism. At lower concentrations (less than100 mM), the direct electron transfer pathway takes place, where the alcohol molecule incorporates the film of Ni hydroxide and become oxidized by the trapped hydroxyl ions [78]. Whereas at higher concentration (>100 mM), the glycerol is chemically consumed, leading to cathodic peak disappearance known as indirect mechanism.

The in-situ PM-IRRAS measurements were conducted to determine the product distribution of GEOR as a function of applied potential. Fig. 5 depicts the spectra obtained during chronoamperometry (CA) measurements at different applied potentials from 0.34 to 5.4 V for 30 min. As mentioned in our previous publications [9,47,48], the spectra illustrate the oxidation species formed on the surface (Fig. 5b) and in the bulk region, i.e., in the electrolyte between the CaF_2 prism and glassy carbon (GC) electrode in Fig. 5b. The presence of a negative band positioned at ~ 1017 cm^{-1} is assigned to C-O stretching of glycerol in KOH solution, thus indicating its consumption during electrooxidation reaction [8]. At all applied potentials, the spectra have mainly four peaks at ~ 1358, 1390, 1430 and 1585 cm^{-1}, corresponding to

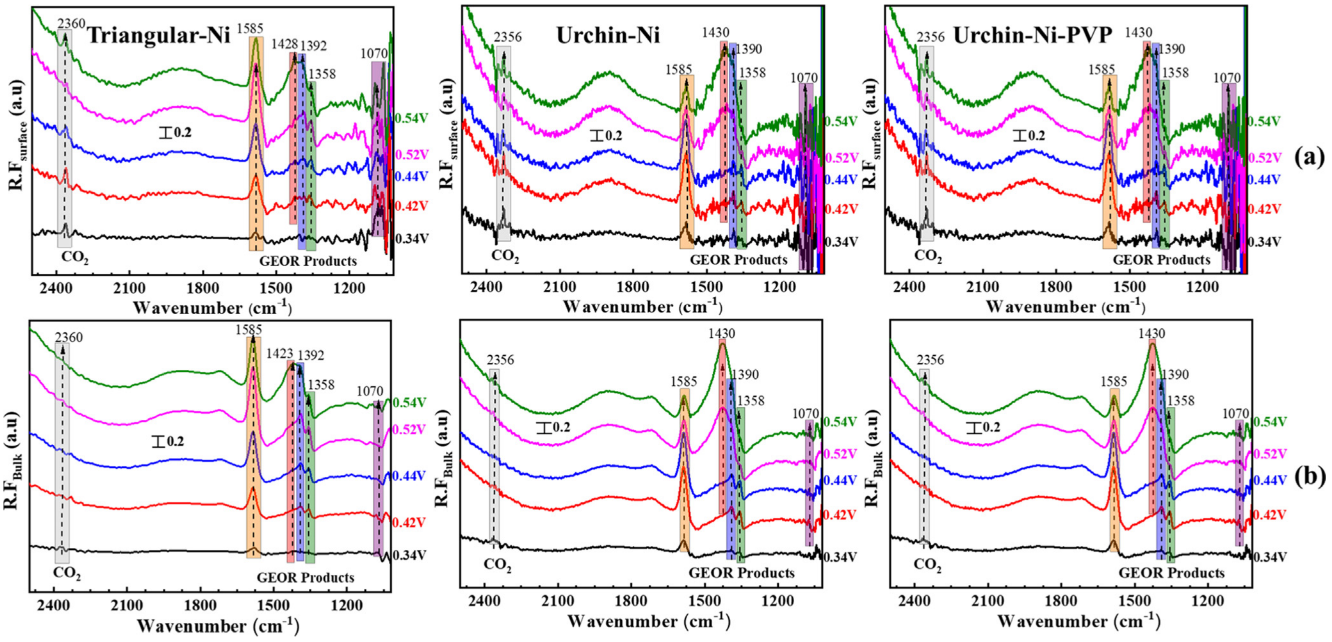

Fig. 5. PM-IRRAS spectra during GEOR on different shapes of Ni NPs. The spectra show oxidation species (a) on the surface and (b) in the bulk/thin cavity solution in 1 M KOH + 0.1 M glycerol at various potentials as indicated in the figure.

symmetric and asymmetric COO^- stretching of formate, carbonate and carboxylate species [76]. These four absorption bands appear on all three different shapes of Ni NPs with different intensities, indicating that the main reaction products do not change. Moreover, a negligible amount of CO_2 was observed due to OH^- consumption, thus changing the interfacial pH to acidic [73]. A similar finding was reported in earlier reports using Ni-based electrocatalysts for GEOR [9,47,48,73–76].

3.3. Theoretical calculations

3.3.1. Energetic and geometric considerations

As shown in Section 3.2, the diffraction ring cannot be fully interpreted due to sample size before reaction and was impossible to be determined under fast reaction conditions (Fig. 2). For this reason, to determine which β-$Ni(OH)_2$ and β-NiOOH surfaces are the most likely to be present during GEOR, we calculated the energies for several low-index surfaces. The results are listed in the Table 1. The obtained values showed that all considered surfaces are stable, where the (001) surface is the most stable in both cases. These results are in good agreement with previous work *Tkalych et al.* [25], *Martirez et al.* [79].

The (001) surface has three possible terminations (facets) in both structures: i) the (001) plane outmost layer can expose H atoms (pristine surface plane), ii) O atoms (plane with surface H atoms removed) or iii) Ni atoms (plane with surface OH groups removed) denoted by (001)-H, (001)-O and (001)-Ni, respectively. Considering that in the reaction process a defective outmost layer is possible we also studied an O-Ni mixed termination (plane with all surface H atoms removed, while only some of the surface O atoms removed) denoted by (001)-mix. The optimized surfaces for β-$Ni(OH)_2$ and β-NiOOH are show in Figs. 6 and 7, respectively.

Table 1
Surface energies of different low index planes for the β-NiOOH and β-$Ni(OH)_2$ phases.

Cleavage planes	E_{surf1} (J/m^2)	
	NiOOH	$Ni(OH)_2$
(100)	0.190	0.735
(010)	0.224	0.675
(001)	0.032	0.019
(011)	0.192	0.126
(101)	0.209	0.583
(102)	0.182	0.112
(111)	1.216	0.202

In these surfaces the usual form of surface energy definition was not suitable. Then, the surface energy for the different surface termination χ (E_{surf2}) was calculated using the following equation:

$$E_{surf2}(\chi) = E_{cl}(\chi) - E_{rel}(\Phi) \quad (4)$$

Where, $E_{cl}(\chi)$ is the cleavage energy, and $E_{rel}(\Phi)$ is the energy of the relaxed surface Φ. $E_{cl}(\chi)$, was computed as:

$$E_{cl}(\chi) = \frac{1}{N_\chi S}\left\{\sum_{\chi=1}^{N_\chi} E_{slab}^{unrel}(\chi) - N_{T.A.}E_{Bulk/Atom}(\Phi)\right\} \quad (5)$$

Where N_χ is the number of considered surface terminations, *S* is the surface area of the slab, and $E_{slab}^{unrel}(\chi)$ is the unrelaxed energy of the χ slab, $N_{T.A.}$ is the total number of atoms contended in all χ slabs.

The relaxed energy of the χ surface, $E_{rel}(\chi)$, was computed as:

$$E_{rel}(\chi) = \frac{1}{2S}\left\{E_{slab}^{rel}(\chi) - E_{slab}^{unrel}(\chi)\right\} \quad (6)$$

Where $E_{slab}^{rel}(\chi)$ is the relaxed energy of the χ slab. For more detailed description see refs [80–84]. The calculated surface energies are listed in Table 2.

In the Ni hydroxide, the surface with mixed Ni and O atoms in the outmost layer is found to be the most stable, however the surface energies vary slightly. This indicates that the removing of all these different atoms from the surface do not change their energy values considerably. Regarding the geometry, the Ni-O and Ni-Ni bond lengths, for L1 on (001)-H surface of $Ni(OH)_2$, are the same that in the bulk 2.08 and 3.16 Å, respectively. These results are in good agreement with experimental and theoretical values reported in the literature [25,85]. In the outmost layer of (001)-O facet Ni-O bond formed with an O atom above (below) the plane line is shortened (elongated) about 2% (1%), while the Ni-Ni bond lengths

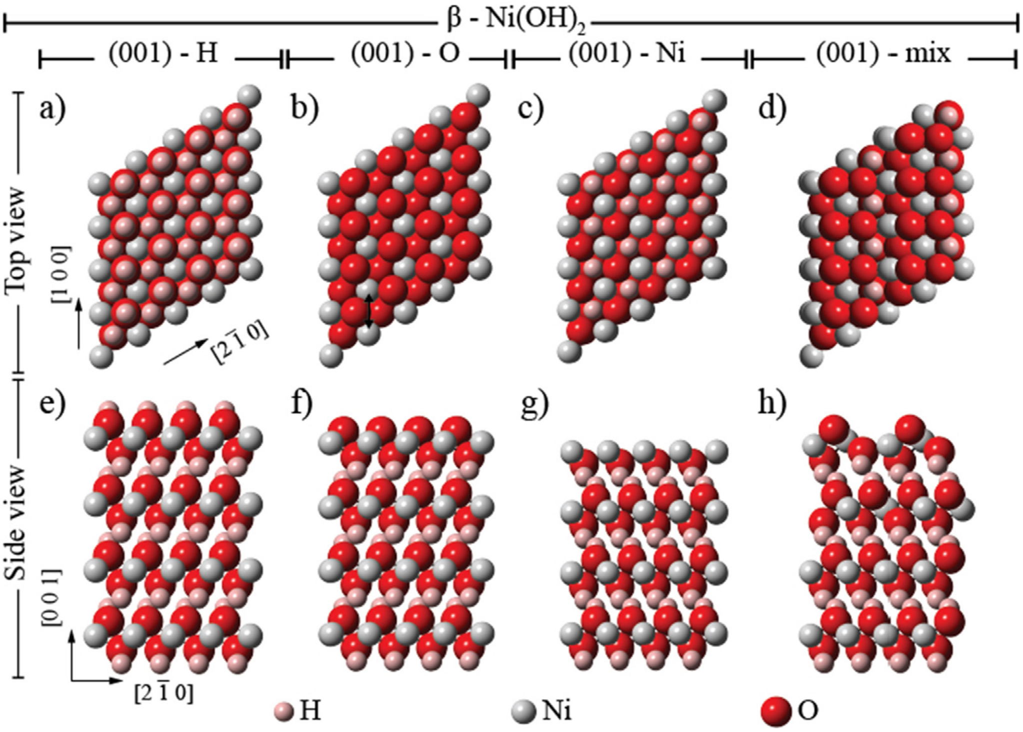

Fig. 6. Top views (top: a, b, c and d) and lateral view (bottom: e, f, g and h) of (001) cleavage plane to the β-Ni(OH)$_2$ system. From the left to the right-side different surface terminations are shown as H exposed (a and e), O exposed (b and f), Ni exposed (c and g) and O&Ni exposed (d and h), named as (001) -H, -O, -Ni and -mix, respectively. For the sake of clarity only the first four layer are show, since the remaining two are bulk like.

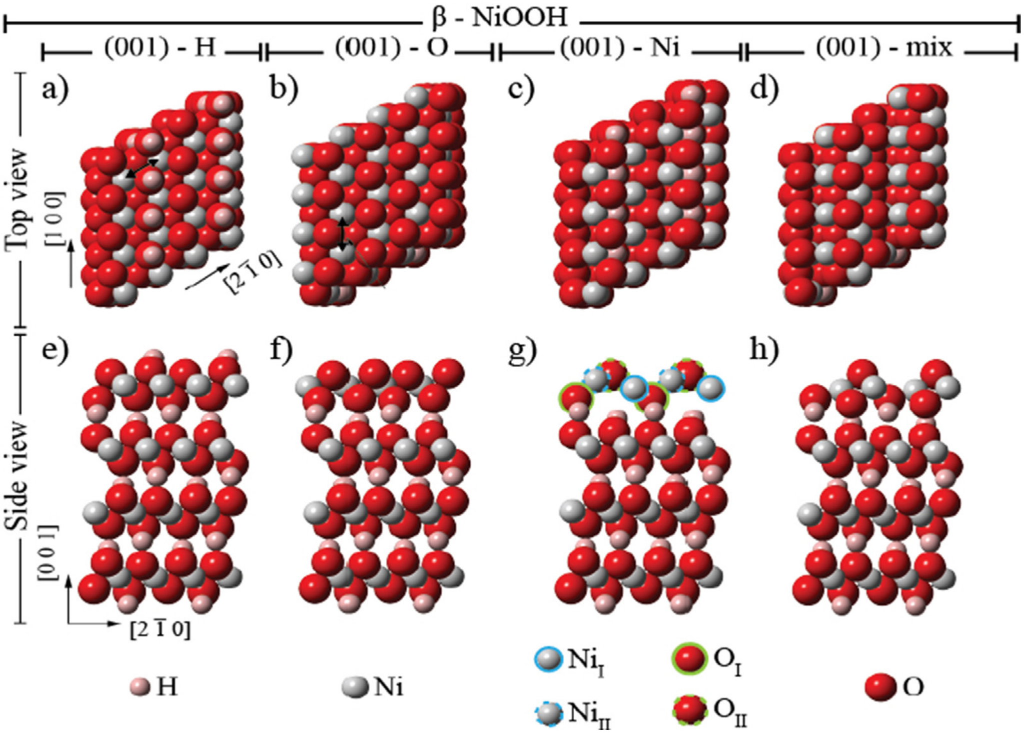

Fig. 7. Top view (top: a, b, c and d) and lateral view (bottom: e, f, g and h) of (001) cleavage plane of the β-NiOOH system. From the left to the right-side different surface terminations are shown as H exposed (a and e), O exposed (b and f), Ni exposed (c and g) and O&Ni exposed (d and h), named as (001)-H, -O, -Ni and -mix, respectively. For the sake of clarity only the first four layer are show, since the remaining two are bulk like.

almost not changes. For the outmost layer of (001)-Ni termination the Ni-Ni remain unchanged, while the Ni-O bond length decrease about 1%. In the case of (001)-mix surface, the Ni-O bond formed by an O atom above (below) the plane line is shortened (elongated) about 4% (3%) and some of the Ni-Ni bond lengths are shortened about 3%. In all cases the bond lengths do not change in the other layers. All these results are consistent with a small reconstruction in the (001)-Mix facet (see Fig. 6). In the case of oxyhydroxide, the

Table 2
Surface energy (E_{surf2}) for different terminations of the (001) cleavage plane for both β-Ni(OH)$_2$ and β-NiOOH systems.

	Cleavage plane termination	$\mathbf{E_{surf2}}$ (eV)
β-Ni(OH)$_2$	(001)-H	0.16
	(001)-O	0.16
	(001)-Ni	0.16
	(001)-mix	0.14
β-NiOOH	(001)-H	0.37
	(001)-O	0.37
	(001)-Ni	−0.17
	(001)-mix	0.35

(001)-H and (001)-O has two Ni-Ni (Ni-O) bonds with distance values of 2.88 and 3.10 Å (1.92 and 2.08 Å), as in the bulk. These results are similar to that reported by *Tkalych et al.* [25] For the outmost layer of (001)-Ni surface the longest and shortest Ni-O bonds lengths decrease about 5% and 7%, respectively. Also, some Ni-Ni bond lengths are elongate about 6%. In the (001)-mix surface, the Ni-O shortest (longest) bonds in L1 not change (decrease about 2%) with respect to that in the bulk, while some Ni-Ni bonds decrease about 4%. The results of the last two facets are consistent with a surface reconstruction, being the most noticeable that on the (001)-Ni surface (see Fig. 7). It is also important to note that the outermost layer is the only affected layer for the cases that present reconstruction. The layers separation is almost unchanged when the different surface terminations are considered for the Ni(OH)$_2$. While in the NiOOH, for the (001)-Ni and -mix facets the L1 and L2 separation is elongated about 7% and 4%, respectively. Also, in the (001)-Ni the L2 and L3 layers separation present a small elongation of 1%. These results agree with the energetic behavior and are consistent with the charge redistribution and electronic structure that will be discussed in the next section.

3.3.2. Electronic structure and magnetic properties

Regarding the electronic structure Figure S6 in SM shows the DOS curves for β-Ni(OH)$_2$ and β-NiOOH. There is a band-gap of about 3 eV for β-Ni(OH)$_2$. This result is similar to other theoretical values reported in the literature [25].

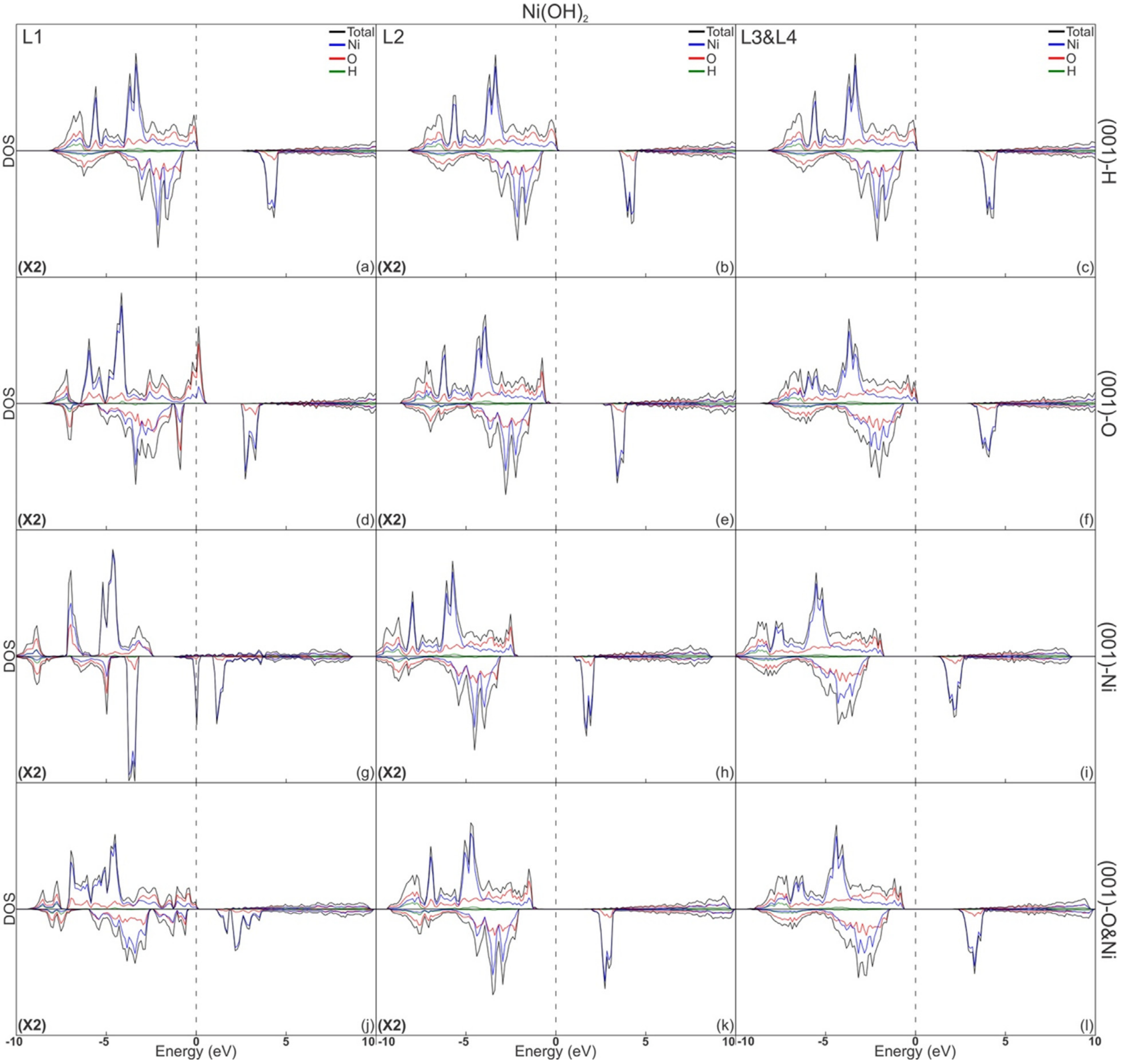

Fig. 8. DOS Curves for the (001) surfaces terminations for the different layers (L1, L2, and L3&L4) for β-Ni(OH)$_2$ phase. The Fermi level is located at 0 eV. For a better view the DOS for single layers are magnified.

From Figure S7 in SM it is clear that the effect of different terminations in the outmost layer of the (001) surface is almost imperceptible in the total DOS curves. For the sake of clarity, we also plotted the layer by layer DOS curves in Figs. 8 and 9 for the (001) surface different terminations of β-Ni(OH)$_2$ and β-NiOOH, respectively. The most significant changes are in the outmost layer (L1) (Fig. 8d, g and j). It can be noted in Fig. 6 that for the second, third, and fourth layers (L2, L3, and L4) the main change in DOS curves is a shift to lower energies for some of the terminations, while for the (001)-H surface the DOS curves are similar to those of the bulk as show in Fig. 8a-c, h, i, k and l (the layers labels are shown in Figs. 10 and 11). This similar DOS and PDOS in (001)-H surface indicates the cleavage keeping the O-H bonds in the surface does not change anything in the electronic structure, and this is a normal cleavage without no important bond broken. Besides the O-H bonds are in the internal bands as it can be seen in the hydrogen PDOS.

Regarding the local magnetic moment, in the (001)-H surface the Ni atoms value is approximately 1.78 μ_B, which is consistent with the Ni^{2+} oxidation state and, as expected, it is similar to that in the bulk. When the superficial hydrogen atoms are removed from the outmost layer, the PDOS of O and Ni nearest to the Fermi level of L1 go to more positive values and the band gap is reduced; in the L2 the band gap increases; and in L3&L4 are the most similar to the bulk DOS. In L1 there is an important reduction on the magnetic moment, while the other layers have a similar value to that in the bulk. In the case of the (001)-Ni surface, only the PDOS-Ni remain in the Fermi level and all the PDOS-O close to it disappear, indicating the O bands near the Fermi level are surface states in (001)-O. In the (001)-Ni the spin up and spin down contributions present different bandgaps, showing the more important decreasing for the spin up contribution in L1, nevertheless in L2 and L3&L4 the behavior is the opposite (Fig. 8g, h and i). The local magnetic moment slightly decreases in the layer L1. This is a consequence of the small increase in the spin down contribution due to a shifted of the DOS curves to lower energies (Fig. 8g). In addition, it can be seen that the outmost layers of (001)-O, (001)-Ni, and (001)-mix surfaces show an increase of DOS states across the Fermi level which could improve the conductivity.

In the case of the β-NiOOH phase, Fig. 9, the (001)-H surface does not show any important changes, but the (001)-O loses an

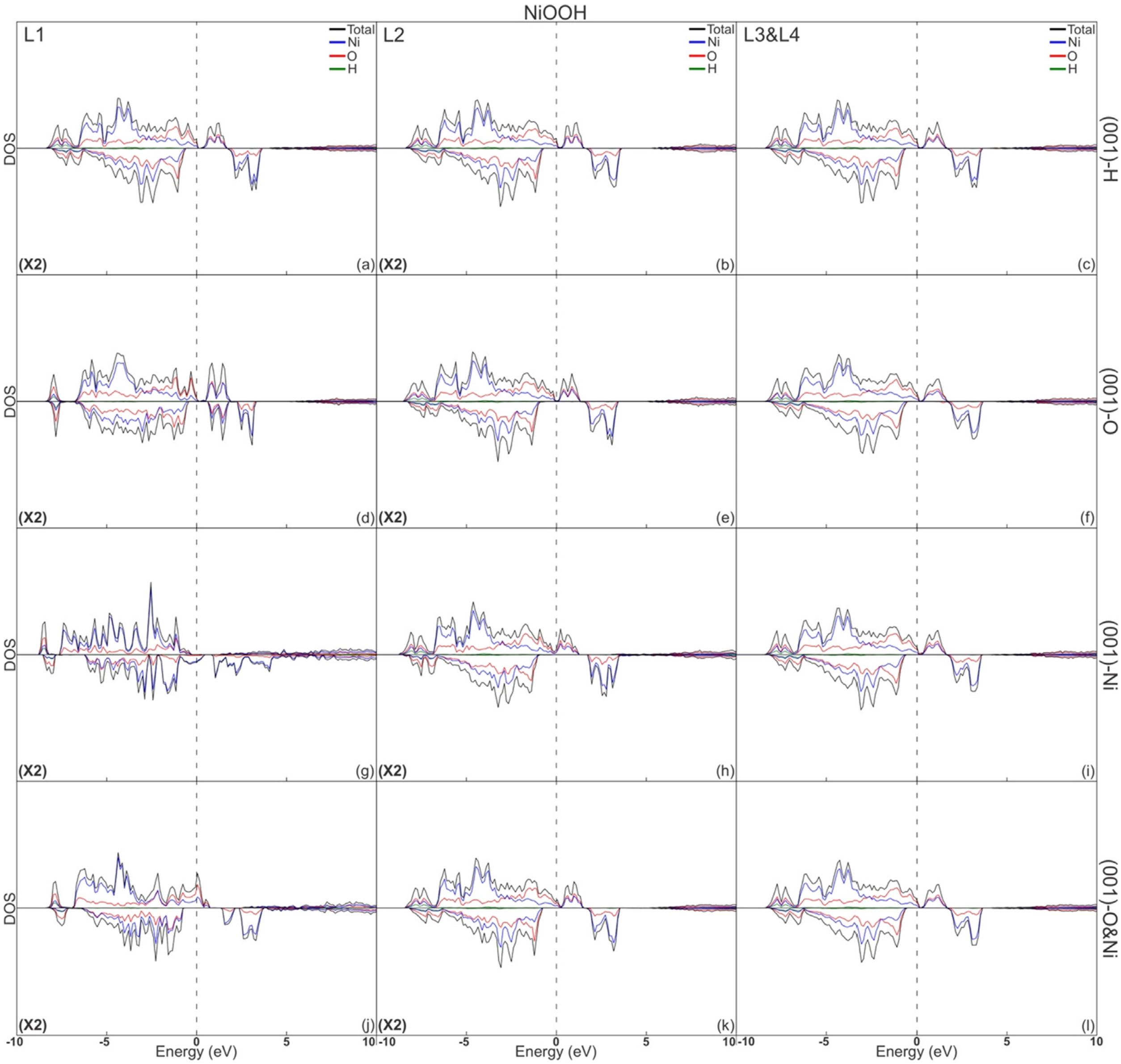

Fig. 9. DOS Curves for the (001) surfaces terminations for β-NiOOH phase. The Fermi level is located at 0 eV. For a better view the DOS for single layers are magnified.

internal PDOS around 7.5 eV, showing a little band gap, so it looks like this lost PDOS corresponds to the O-H bond. In general, all DOS of Fig. 9 shown that only the outmost layer of each termination presents changes, while the other layers are almost the same. For the first layer, all systems have states across the Fermi level, being the (001)-Ni and (001)-mix surfaces those with more states around E_F, which could indicate an improvement in the conductivity of these systems. Considering the magnetic behavior, the (001)-H outmost layer is similar to that in the bulk. For (001)-O an important reduction in the local magnetic moment appeared. This is a consequence of the different oxidation states of the superficial Ni atoms due to the removal of H. In this surface, some superficial Ni atoms have a value of 1.10 μ_B consistent with Ni^{3+} oxidation state, while others have an amount of 0.05 μ_B that correspond to a Ni^{4+} oxidation state. In the case of (001)-Ni plane, some of the surface Ni from the outmost layer have an increase in the local magnetic moment resulting in a value of 1.68 μ_B, while in the others the value is 1.28 μ_B, which are consistent with a Ni^{2+} and Ni^{3+} oxidation states, respectively. These results are in a good agreement with the results reported by *Fildesky et al* and *Bender et al* [86,87]. Regarding the center of the *d*-band energy in both systems the (001)-Ni and (001)-mix surfaces are more reactive with an ε_d close to the Fermi level, with the (001)-Ni surface for the Ni oxyhydroxide being the closest one.

3.3.3. Charge transfer

Figs. 10 and 11 show the layer-by-layer net charge transferred (into the smallest super-cell containing four Ni per layer) and onto the individual atoms in the cross section (upper and lower part of each one of the subfigures, respectively) for the last four of the (001) cleavage plane for both β-$Ni(OH)_2$ and β-NiOOH systems, respectively. In the bottom part of these figures, a darker blue color indicates more electron accumulation, while a darker red color indicates electron depletion (crossing through the white tone that indicates no electron transference). For each system, the four different terminations of this cleavage plane are shown (from left to right side, named as the (001)-H, (001)-O, (001)-Ni and (001)-mix). From these figures, it is clear that varying the cleavage plane composition, only the outmost layer is considerably affected in both systems. The charge is not equally distributed onto the atoms within the same layer, almost all of the charge transfer occurs between nickel and oxygen atoms, where the oxygen atoms gain electrons at the expense of hydrogen and nickel atoms, which lose electrons.

In the β-$Ni(OH)_2$ system, the (001)-H surface has similar charge distribution for all layers. The H and Ni atoms lose 1.00 and ~ 1.35 e^-, respectively; while the O atoms gains ~ 1.70 e^- (Fig. 10a and e). For the outmost layer (L1) in the other three surfaces terminations, the Ni lose around 1.40, 1.25 and 0.71 e^-, respectively; while the lower (upper) O gain ~ 1.70 e^- (~1.00 e^-) (see Figs. 10 and 6f-h).

In the case of the β-NiOOH system, it can be seen that the hydrogen atoms lose 1.00 e^- for all terminations (Fig. 11e, f, g and h). In the case of (001)-H surface a similar charge distribution for all layers was observed, but the behaviour of O and Ni atoms differed slightly with respect to β-$Ni(OH)_2$, depending on if they are bonded to a hydrogen or not: the upper O atoms bond gain around 1.57 and 0.89 e^- and the lower O gain 1.54 and 0.93 e^-, respectively. Meanwhile, the Ni atoms lose around 1.47 e^- (Fig. 11a and e, and 7e). For the (001)-O termination, the upper (lower) O atoms gain between 0.75 and 0.81 e^- (1.45 and 0.93 e^-), while the Ni atoms lose around 1.45 and 1.51 e^-, depending on if the lower oxygen is binding to a hydrogen or not (Fig. 11b and f, and Fig. 7f). In the (001)-mix system, the upper O won 0.97 e^-, and the upper Ni lose 1.25 e^-, while the nickel below the oxygen lost 1.32 e^-. The lower O atoms gain 1.58 and 1.05 e^-, depending on if they are bonded to a hydrogen or not (Fig. 11d and h, and 7 h). The (001)-Ni surface presents an important reconstruction in the outmost layer and an important charge distribution (Fig. 11c and g). The O atoms bonded to an hydrogen remain close to their unrelaxed position (remarked with a green full circle denoted by O_I in Fig. 7g gain around 1.65 e^-, while the O atoms that shifted significantly of their position (remarked with a green dashed circle and denoted by O_{II} in Fig. 7g) gain about 1.18 e^-. The Ni bonded to the O_I atoms (remarked with a light blue full line

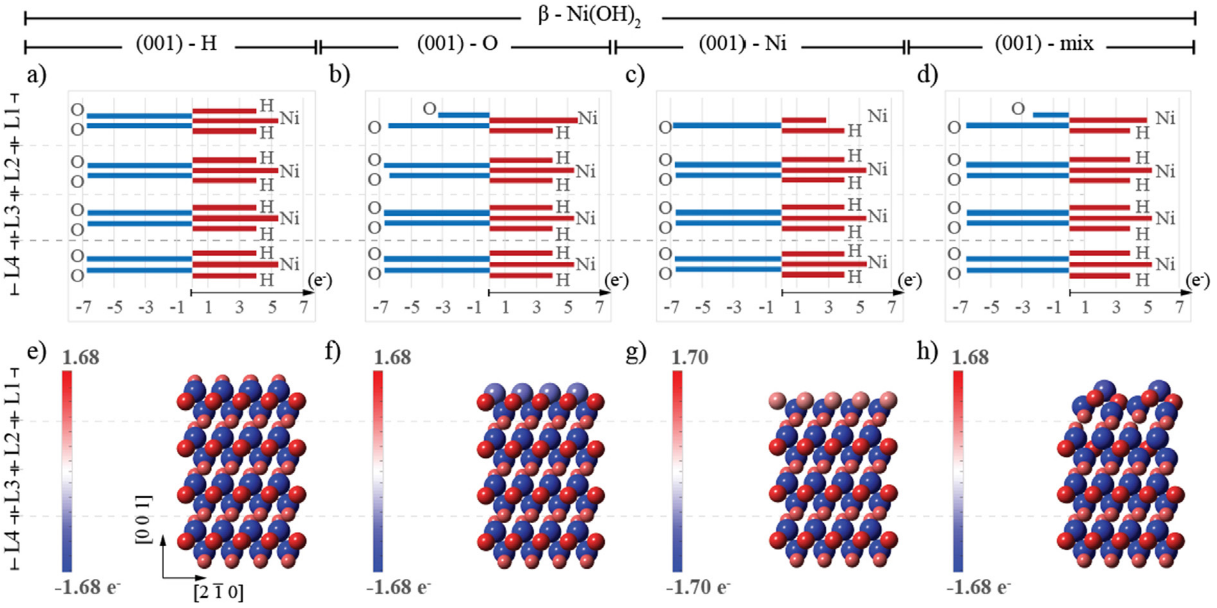

Fig. 10. Electron charge transfer of (001) cleavage plane to the β-$Ni(OH)_2$ system of the different surface termination are shown from the left to the right side, as (001)-H (a and e), (001)-O (b and f), (001)-Ni (c and g) and (001)-mix (d and h). The upper part of the figure (a, b, c and d) shows layer-by-layer charge transferred as sort in the lower part (e, f, g and h). The lateral view in the lower part shown the electron charge transferred atom by atom. Starting from the outmost to the inner the layers are called L1, L2, L3 and L4, respectively. The charge is in units of e^-.

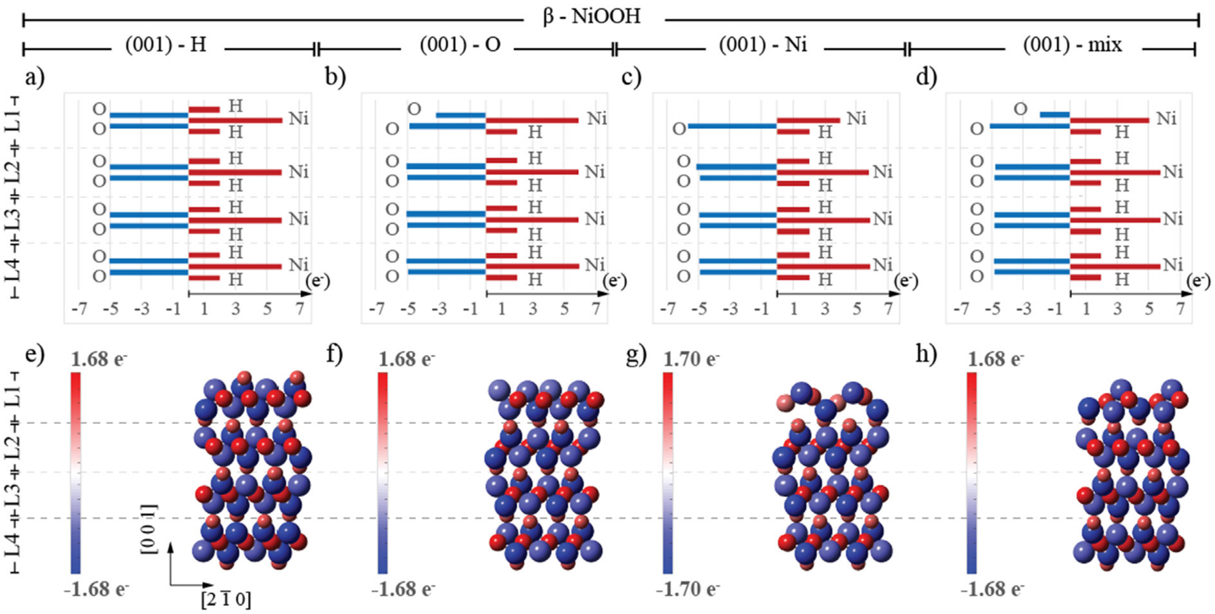

Fig. 11. Electron charge transfer of (001) cleavage plane to the β-NiOOH system of the different surface termination are shown from the left to the right side, as (001)-H (a and e), (001)-O (b and f), (001)-Ni (c and g) and (001)-mix (d and h). The upper part of the figure (a, b, c and d) shows layer-by-layer charge transferred as sort in the lower part (e, f, g and h). The lateral view in the lower part shown the electron charge transferred atom by atom. L1, L2, L3 and L4 denote the outmost layer, the one that follows and so on, respectively. The charge transfer is in units of e^-.

denoted by Ni_I in Fig. 7g) lose around 0.81 e^- and the others nickels (remarked with a light blue dashed circle denoted by Ni_{II} in Fig. 7g) lose about 1.16 e^- (Fig. 11c and g).

In summary, the electronic structure and charge transfer results show that the layer interactions in both systems are weak. In addition, in the case of β-NiOOH different terminations affect the local magnetic moment and the transferred charge of surface Ni atoms. These results are consistent with Ni^{+3} and Ni^{+4} oxidation states present in the systems. These facts could explain experimental results without considering a multiphase composition of the sample, and also could indicate that during the reaction process a transfer of both electrons and protons occur. The increase in the DOS around the Fermi level and the *d*-band results suggests that the surface is reactive and could be suitable candidate for the electrooxidation of glycerol to occur.

4. Conclusion

Different electron microscopy characterization techniques have shown the conversion of monometallic Ni to Ni hydroxides during cyclic voltammetry causing a volume expansion of particles. Effectively, nickel hydroxide is formed on the shell while nickel remains in the core. The presence of both phases is demonstrated with electron diffraction. The electrochemical oxidation of glycerol in alkaline media showed the catalytic activity of mono-metallic Ni catalyst depends on the morphology and decreases as Ni-urchin-PVP > Ni-urchin > Ni-triangular in a potential range higher than 0.4 V vs. Hg/HgO. All different shape-controlled microstructures either follow indirect electron transfer mechanism at higher glycerol concentration ≥ 100 mM or the direct electron transfer pathway at low concentration. *In-situ* infrared spectroscopy measurements illustrated those main products are mainly symmetric and asymmetric COO^- stretching of formate, carbonate and carboxylate species with no significant effect for GEOR reaction pathway.

Our computational models propose a way to connect NP of about 10 nm or more with a particular plane using a plausible experimental structure. DFT calculations of the oxy-hydroxide compounds indicated that the most stable plane in β-NiOOH is (001)-Ni as a metallic state presenting an important surface reconstruction, which is consistent with DOS change and charge transfer. This characteristic makes it a favorable active surface for GEOR. In addition, from the magnetic moments extracted from the PDOS, the surface termination exposes a mix of Ni^{+3} and Ni^{+4} oxidation states representing an interesting couple that may be responsible for electrochemical reactivity of Ni-based materials. The computed map of electronic charges on the surfaces showed an increase in the global electron density and the present of Ni cations and O anions and the same height after reconstruction. These facts could supply useful sites for glycerol OH groups interaction under electrooxidation. This will be subject of the future works.

Declaration of Competing Interest

The authors declare that they have no known competing financial interests or personal relationships that could have appeared to influence the work reported in this paper.

Acknowledgements

This paper was partially supported by grants of CONICET (Argentina National Research Council), Universidad Nacional del Sur (UNS) and by ANPCyT through PICT 4085, and PIP-CONICET Nos. 11220130100436 research grant, as well as by SGCyT- UNS., E. A. G., P. V. J., M. G. S. and A. J. are members of CONICET., F. E and F. G. are fellow researchers at this institution. The authors acknowledge Ni Electro Can project administered from Queen's University and supported by "Grant No. RGPNM 477963-2015 under the Natural Sciences and Engineering Research Council of Canada (NSERC) Discovery Frontiers Program. The support by MinCyT and UOttawa research grant is also acknowledged for travel funds to Universidad Nacional del Sur. M. G. S., A. H.-L. and C. I. S.-D. do thank to Dr. Santiago Melchor Ferrer from the University of Granada for important assistances to the DFT calculations; and A. H.-L. and C. I. S.-D. acknowledge the Spanish MINCINN project grants FIS2016-77692-C2-2P and PCIN-2017-098, along with FEDER European funds; we also thank to the Alhambra Computing Center (University of Granada, Spain) for important CPU time.

Appendix A. Supplementary material

Supplementary data to this article can be found online at https://doi.org/10.1016/j.jcat.2021.10.010.

References

[1] C. Liu, M. Hirohara, T. Maekawa, R. Chang, T. Hayashi, C.Y. Chiang, Selective electro-oxidation of glycerol to dihydroxyacetone by a non-precious electrocatalyst – CuO, Appl. Catal. B 265 (2020) 118543.

[2] R.M. Castagna, J.M. Sieben, A.E. Alvarez, M.M. Duarte, Electrooxidation of ethanol and glycerol on carbon supported PtCu nanoparticles, Int. J. Hydrogen Energy 44 (2019) 5970–5982.

[3] S. Dash, N. Munichandraiah, Nanoflowers of PdRu on PEDOT for Electrooxidation of Glycerol and Its Analysis, Electrochim. Acta 180 (2015) 339–352.

[4] G. Dodekatos, S. Schünemann, H. Tüysüz, Recent Advances in Thermo-, Photo-, and Electrocatalytic Glycerol Oxidation, ACS Catal. 8 (7) (2018) 6301–6333.

[5] M. Martin, Diesel fuel derived from vegetable oils, VI: Specifications and quality control of biodiesel, Bioresource Technol. 56 (1996) 7–11.

[6] S.G. Silva, F.R.P. Rocha, A flow injection procedure based on solenoid micro-pumps for spectrophotometric determination of free glycerol in biodiesel, Talanta 83 (2010) 559–564.

[7] P.A. Alaba, C.S. Lee, F. Abnisa, M.K. Aroua, P. Cognet, Y. Pérès, W.M.A.W. Daud, A review of recent progress on electrocatalysts toward efficient glycerol electrooxidation, Rev. Chem. Eng. 20190013 (2020), https://doi.org/10.1515/revce-2019-0013.

[8] M. Simoes, S. Baranton, C. Coutanceau, Electrochemical Valorization of Glycerol, ChemSusChem 5 (2012) 2106–2124.

[9] M.S.E. Houache, E. Cossar, S. Ntais, E.A. Baranova, Electrochemical modification of nickel surfaces for efficient glycerol electrooxidation, J. Power Sources 375 (2018) 310–319.

[10] M.S.E. Houache, K. Hughes, E.A. Baranova, Study on catalyst selection for electrochemical valorization of glycerol, Sustain. Energy Fuels 3 (2019) 1892–1915.

[11] K. Subramanyam, N. Sreelekha, D.A. Reddy, G. Murali, K.R. Varma, R.P. Vijayalakshmi, Chemical synthesis, structural, optical, magnetic characteristics and enhanced visible light active photocatalysis of Ni doped CuS nanoparticles, Solid State Sci. 65 (2017) 68–78.

[12] S. Ni, X. Lv, T. Li, X. Yang, L. Zhang, The investigation of $Ni(OH)_2$/Ni as anodes for high performance Li-ion batteries, J. Mater. Chem. A 1 (5) (2013) 1544–1547.

[13] J. Yan, Z. Fan, W. Sun, G. Ning, T. Wei, Q. Zhang, R. Zhang, L. Zhi, F. Wei, Advanced Asymmetric Supercapacitors Based on $Ni(OH)_2$/Graphene and Porous Graphene Electrodes with High Energy Density, Adv. Funct. Mater. 22 (12) (2012) 2632–2641.

[14] J. Jeon, H.B.R. Lee, Z. Bao, Flexible Wireless Temperature Sensors Based on Ni Microparticle-Filled Binary Polymer Composites, Adv. Mater. 25 (6) (2013) 850–855.

[15] A. Allagui, S. Sarfraz, E. A. Baranova. $NiXPd_{1-x}$ (x=0.98, 0.93, and 0.58) nanostructured catalysts for ammonia electrooxidation in alkaline media, Electrochimica Acta, 110, 253–259.

[16] L. Chen, L. Lu, H. Zhu, Y. Chen, Y. Huang, Y. Li, L. Wang. Regular-triangle trimer and charge order preserving the Anderson condition in the pyrochlore structure of CsW_2O_6, Nature Communications, 2020, 11(1), 1–1.

[17] T. Eisa, H.O. Mohamed, Y.J. Choi, S.G. Park, R. Ali, M.A. Abdelkareem, S.E. Oh, K.J. Chae, Nickel nanorods over nickel foam as standalone anode for direct alkaline methanol and ethanol fuel cell, Int. J. Hydrogen Energy 45 (10) (2020) 5948–5959.

[18] X. Hou, L. Qi, W. Li, J. Zhao, S. Liu, Theoretical study on water adsorption and dissociation on the nickel surfaces, J. Mol. Mod. 27 (2021) 36.

[19] H. Bode, K. Dehmelt, J. Witte, Zur kenntnis der nickelhydroxidelektrode—I. Über das nickel (II)-hydroxidhydrat, Electrochimca Acta 11 (1966) 1079–1087.

[20] H. Bode, K. Dehmelt, J. Witte, Zur Kenntnis der Nickelhydroxidelektrode. II. Über die Oxydationsprodukte von Nickel(II)-hydroxiden, Z. Anorg. Allg. Chem. 366 (1–2) (1969) 1.

[21] X. Yang, K. Takada, M. Itose, Y. Ebina, R. Ma, K. Fukuda, T. Sasaki, Highly Swollen Layered Nickel Oxide with a Trilayer Hydrate Structure, Chem. Mater. 20 (2008) 479–485.

[22] A. Van der Ven, D. Morgan, Y.S. Meng, G. Ceder, Phase Stability of Nickel Hydroxides and Oxyhydroxides, J. Electrochem. Soc. 153 (2006) A210–A215.

[23] S. Park, Y. Lee, M. Elcombe, T. Vogt, Synthesis and Structure of the Bilayer Hydrate $Na_{0.3}NiO_2\cdot 1.3D_2O$, Inorg. Chem. 45 (2006) 3490–3492.

[24] L. Guerlou-Demourgues, C. Delmas, Electrochemical Behavior of the Manganese-Substituted Nickel Hydroxides, J. Electrochem. Soc. 143 (1996) 561–566.

[25] A.J. Tkalych, K. Yu, E.A. Carter, Structural and Electronic Features of β-$Ni(OH)_2$ and β-NiOOH from First Principles, J. Phys. Chem. C 119 (43) (2015) 24315–24322.

[26] A. Szytula, A. Murasik, M. Balanda, Phys. Status Solidi B 43 (1971) 125–128.

[27] M. Casas-Cabanas, J. Canales-Vazquez, J. Rodriguez-Carvajal, M.R.J. Palacin, Deciphering the Structural Transformations during Nickel Oxyhydroxide Electrode Operation, J. Am. Chem. Soc. 129 (2007) 5840–5842.

[28] M. Rajamathi N. G. Subbanna, P. V. Kamath. On the existence of a nickel hydroxide phase which is neither α nor β, J. Mater. Chem., 1997, 7, 2293–2296.

[29] Q. Song, Z. Tang, H. Guo, S.L.I. Chan, $Ni(OH)_2$ particles synthesized by high energy ball milling, J. Power Sources 112 (2002) 428–434.

[30] F.P. Kober, Analysis of the charge–discharge characteristics of nickel-oxide electrodes by infrared spectroscopy, J. Electrochem. Soc 112 (1965) 1064–1067.

[31] C. Faure, Y. Borthomieu, C. Delmas, Infrared characterization of turbostratic α- and well crystallized α*-cobalted nickel hydroxides, J. Power Sources 36 (1991) 113–125.

[32] M. Dixit, P.V. Kamath, J. Gopalakrishnan, Zinc-Substituted α-Nickel Hydroxide as an Electrode Material for Alkaline Secondary Cells, J. Electrochem. Soc. 146 (1999) 79–82.

[33] K.I. Pandya, W. O'Grady, D.A. Corrigan, J. McBreen, R.W. Hoffman, Extended x-ray absorption fine structure investigations of nickel hydroxides, J. Phys. Chem. 94 (1) (1990) 21–26.

[34] A.F. Wells, Structural Inorganic Chemistry, Oxford University Press, London, 1975, pp. 257–259.

[35] M. Rajamathi, P. Vishnu Kamath, R. Seshadri, Polymorphism in nickel hydroxide: role of interstratification, J. Mater. Chem. 10 (2000) 503–506.

[36] P.V. Kamath, M. Dixit, L. Indira, A.K. Shukla, V.G. Kumar, N. Munichandraiah, Stabilized α-$Ni(OH)_2$ as Electrode Material for Alkaline Secondary Cells, J. Electrochem. Soc. 141 (1994) 2956–2959.

[37] U.M. Patil, K.V. Gurav, V.J. Fulari, C.D. Lokhande, O.S. Joo, Characterization of honeycomb-like "β-$Ni(OH)_2$" thin films synthesized by chemical bath deposition method and their supercapacitor application, J. Power Sources 188 (2009) 338–342.

[38] M.K. Carpenter, D.A. Corrigan, Photoelectrochemistry of Nickel Hydroxide Thin Films, J. Electrochem. Soc. 136 (1989) 1022–1026.

[39] P. Oliva, J. Leonardi, J.F. Laurent, C. Delmas, J.J. Braconnier, M. Figlarz, F. Fievet, A. Guibert, Review of the structure and the electrochemistry of nickel hydroxides and oxy-hydroxides, J. Power Sources 8 (1982) 229–255.

[40] T.W. Capehart, D.A. Corrigan, R.S. Conell, K.I. Pandya, R.W. Hoffman, *In situ* extended x-ray absorption fine structure spectroscopy of thin-film nickel hydroxide electrodes, Appl. Phys. Lett. 58 (1991) 865–867.

[41] J. McBreen, The Nickel Oxide Electrode, In Modern Aspects of Electrochemistry Plenum Press, New York, 1990, pp. 29–63.

[42] K.I. Pandya, R.W. Hoffman, J. McBreen, W. O'Grady, *In Situ* X-Ray Absorption Spectroscopic Studies of Nickel Oxide Electrodes, J. Electrochem. Soc. 137 (1990) 383–388.

[43] Y. Li, A. Selloni, Mosaic Texture and Double *c*-Axis Periodicity of β-NiOOH: Insights from First-Principles and Genetic Algorithm Calculations, J. Phys. Chem. Lett. 5 (2014) 3981–3985.

[44] M.J. Madou, M.C.H. McKubre, Impedance Measurements and Photoeffects on Ni-Electrodes, J. Electrochem. Soc. 130 (1983) 1056–1061.

[45] M.K. Canperter, D.A. Corrigan, Photoelectrochemistry of Nickel hydroxide thin film, J. Electrochem. Soc. 136 (4) (1989) 1022.

[46] R.P. Lamsal, M.S. Houache, A. Williams, E. Baranova, G. Jerkiewicz, D. Beauchemin, Single particle inductively coupled plasma mass spectrometry with and without flow injection for the characterization of nickel nanoparticles, Anal. Chim. Acta 1120 (2020) 67–74.

[47] M.S.E. Houache, K. Hughes, A. Ahmed, R. Safari, H. Liu, G.A. Botton, E.A. Baranova, Electrochemical Valorization of Glycerol on Ni-Rich Bimetallic NiPd Nanoparticles: Insight into Product Selectivity Using in Situ Polarization Modulation Infrared-Reflection Absorption Spectroscopy, ACS Sustainable Chem. Eng. 7 (2019) 14425–14434.

[48] M.S. Houache, K. Hughes, R. Safari, G.A. Botton, E.A. Baranova, Modification of Nickel Surfaces by Bismuth: Effect on Electrochemical Activity and Selectivity toward Glycerol, ACS Appl. Mater. Interfaces 12 (13) (2020) 15095–15107.

[49] P.E. Blöchl, Projector Augmented-Wave Method, Phys. Rev. B 50 (1994) 17953–17979.

[50] G. Kresse, D. Joubert, From ultrasoft pseudopotentials to the projector augmented-wave method, Phys. Rev. B 59 (1999) 1758–1775.

[51] G. Kresse, J. Hafner, *Ab initio* molecular dynamics for liquid metals, Phys. Rev. B 47 (1993) 558–561.

[52] G. Kresse, J. Furthmüller, Efficiency of ab-initio total energy calculations for metals and semiconductors using a plane-wave basis set, Mater. Sci. 6 (1996) 15–20.

[53] J.P. Perdew, K. Burke, M. Ernzerhof, Generalized gradient approximation made simple, Phys. Rev. Lett. 77 (1996) 3865–3868.

[54] S.L. Dudarev, G.A. Botton, S.Y. Savrasov, C.J. Humphreys, A.P. Sutton, Electron-energy-loss spectra and the structural stability of nickel oxide: an LSDA + U study, Phys. Rev. B 57 (1998) 1505–1509.

[55] M. Casas-Cabanas, M.D. Radin, J. Kim, C.P. Grey, A. Van der Ven, M. Rosa Palacín, The nickel battery positive electrode revisited: stability and structure of the β-NiOOH phase, J. Mater. Chem. A 6 (2018) 19256–19265.

[56] H.J. Monkhorst, J.D. Pack, Special points for Brillouin-zone integrations, Phys. Rev. B 13 (1976) 5188–5192.

[57] C. Greaves, M.A. Thomas, Refinement of the structure of deuterated nickel hydroxide, Ni(OD)$_2$, by powder neutron diffraction and evidence for structural disorder in samples with high surface area, Acta Crystallogr. B 42 (1986) 51–55.

[58] V.Y. Kazimirov, M.B. Smirnov, L. Bourgeois, L. Guerlou-Demourgues, L. Servant, A.M. Balagurov, I. Natkaniec, N.R. Khasanova, E.V. Antipov, Atomic structure and lattice dynamics of Ni and Mg hydroxides, Solid State Ionics 181 (2010) 1764–1770.

[59] Q. Song, Z. Tang, H. Guo, S.L.I.J. Chan, Structural characteristics of nickel hydroxide synthesized by a chemical precipitation route under different pH values, J. Power Sources 112 (2002) 428–434.

[60] C. Tessier, P.H. Haumesser, P. Bernard, C.J. Delmas, The Structure of Ni(OH)$_2$: From the Ideal Material to the Electrochemically Active One, J. Electrochem. Soc. 146 (1999) 2059–2067.

[61] N.R.S. Farley, S.J. Gurman, A.R. Hillman, Dynamic EXAFS study of discharging nickel hydroxide electrode with non-integer Ni valency, Electrochim. Acta 46 (2001) 3119–3127.

[62] F. Baletto, R. Ferrando, Structural properties of nanoclusters: Energetic, thermodynamic, and kinetic effects, Rev. Mod. Phys. 77 (2005) 371–417.

[63] R. Miotto, F.D. Kiss, A.C. Ferraz, Changes in a nanoparticle's spectroscopic signal mediated by the local environment, Nanotechnology 23 (2012) 485202–485208.

[64] F.D. Kiss, R. Miotto, A.C. Ferraz, Size effects on silver nanoparticles' properties, Nanotechnology 22 (2011) 275708–275717.

[65] A. Ruban, B. Hammer, P. Stoltze, H.L. Skriver, J.K. Nørskov, Surface electronic structure and reactivity of transition and noble metals, J. Mol. Catal. A 115 (1997) 421–429.

[66] B. Hammer, J.K. Nørskov, Electronic factors determining the reactivity of metal surfaces, Surf. Sci. 343 (1995) 211–220.

[67] B. Hammer, J.K. Nørskov, Why gold is the noblest of all the metals, Nature 376 (1995) 238–240.

[68] B. Hammer, J.K. Nørskov, Theoretical surface science and catalysis-calculations and concepts, Adv. Catal. 45 (2000) 71–129.

[69] R.F.W. Bader, Atoms in Molecules - A Quantum Theory, Oxford University Press, 1990.

[70] W. Tang, E. Sanville, G. Henkelman, A grid-based Bader analysis algorithm without lattice bias, J. Phys.: Condens., Matter 21 (8) (2009) 084204.

[71] E. Cossar, M.S.E. Houache, Z. Zhang, E.A. Baranova, Journal of Electroanalytical Chemistry, Comparison of electrochemical active surface area methods for various nickel nanostructures 870 (2020) 114246.

[72] E. G. Neiva, M. F. Bergamini, M. M. Oliveira, Jr L. H. Marcolino A. J. Zarbin. PVP-capped nickel nanoparticles: Synthesis, characterization and utilization as a glycerol electrosensor, Sensors and Actuators B: Chemical, 2014, 196, 574–581.

[73] V.L. Oliveira, C. Morais, K. Servat, T.W. Napporn, G. Tremiliosi-Filho, K.B. Kokoh, Glycerol oxidation on nickel based nanocatalysts in alkaline medium – Identification of the reaction products, J. Electroanal. Chem. 703 (2013) 56–62.

[74] V.L. Oliveira, C. Morais, K. Servat, T.W. Napporn, G. Tremiliosi-Filho, K.B. Kokoh, Studies of the reaction products resulted from glycerol electrooxidation on Ni-based materials in alkaline medium, Electrochim. Acta. 117 (2014) 255–262.

[75] V.L. Oliveira, C. Morais, K. Servat, T.W. Napporn, P. Olivi, K.B. Kokoh, G. Tremiliosi-Filho, Kinetic Investigations of Glycerol Oxidation Reaction on Ni/C, Electrocatalysis 6 (2015) 447–454.

[76] J.L. Bott-Neto, T.S. Martins, S.A. Machado, E.A. Ticianelli, Electrocatalytic Oxidation of Methanol, Ethanol, and Glycerol on Ni(OH)$_2$ Nanoparticles Encapsulated with Poly[Ni(*salen*)] Film, ACS Appl. Mater. Interfaces 11 (2019) 30810–30818.

[77] M. Fleischmann, K. Korinek, D. Pletcher, The oxidation of organic compounds at a nickel anode in alkaline solution, J. Electroanal. Chem. Interfacial Electrochem 31 (1971) 39–49.

[78] J. Taraszewska, G. Rosłonek, Electrocatalytic oxidation of methanol on a glassy carbon electrode modified by nickel hydroxide formed by ex situ chemical precipitation, J. Electroanal. Chem. 364 (1994) 209–213.

[79] J.M.P. Martirez, E.A. Carter, Effects of the Aqueous Environment on the Stability and Chemistry of β-NiOOH Surfaces, Chem. Mater. 30 (2018) 5205–5219.

[80] R.I. Eglitis, *Ab initio* hybrid DFT calculations of BaTiO$_3$, PbTiO$_3$, SrZrO$_3$ and PbZrO$_3$(111) surfaces, Appl. Surf. Sci. 358 (2015) 556–562.

[81] Y. Takagi, T. Yamada, M. Yoshino, T. Nagasaki, *Ab initio* Study on Face Azimuth Dependency of Surface Energy and Structure in PbTiO$_3$, Ferroelectrics 490 (1) (2016) 167–173.

[82] X. Tian, T. Wang, L. Fan, Y. Wang, H. Lu, Y. Mu, A DFT based method for calculating the surface energies of asymmetric MoP facets, Appl. Surf. Sci. 427 (2018) 357–362.

[83] K. Choudhary, A.J. Biacchi, S. Ghosh, L. Hale, A.R.H. Walker, F. Tavazza, High-throughput assessment of vacancy formation and surface energies of materials using classical force-fields, J. Phys. Condens. Matter 30 (39) (2018) 395901.

[84] M. Šilhavý, The general form of the relaxation of a purely interfacial energy for structured deformations, Math. Mech. Complex Syst. 5 (2) (2017) 191–215.

[85] K.I. Pandya, R.W. Hoffman, J. McBreen, W. O'Grady, *In Situ* X-Ray Absorption Spectroscopic Studies of Nickel Oxide Electrodes, J. Electrochem. Soc. 137 (1990) 383–388.

[86] V. Fidelsky, D. Furman, Y. Khodorkovsky, Y. Elbaz, Y. Zeiri, M.C. Toroker, Electronic structure of β-NiOOH with hydrogen vacancies and implications for energy conversion applications, MRS Commun. 7 (2) (2017) 206–213.

[87] M.T. Bender, Y.C. Lam, S. Hammes-Schiffer, K.-S. Choi, Unraveling Two Pathways for Electrochemical Alcohol and Aldehyde Oxidation on NiOOH, J. Am. Chem. Soc. 142 (51) (2020) 21538–22154.